J. Micromech. Microeng. **17** (2007) 1558–1566 doi:10.1088/0960-1317/17/8/019

# Compound jet instability in a microchannel for mononuclear compound drop formation

**S Y Lee[1,2], C Snider[2,3], K Park[2,4] and J P Robinson[1,2,4]**

[1] Department of Basic Medical Sciences, Purdue University, W Lafayette, IN 47907, USA
[2] Bindley Bioscience Center, Purdue University, W Lafayette, IN 47907, USA
[3] Department of Industrial and Physical Pharmacy, Purdue University, W Lafayette, IN 47907, USA
[4] Weldon School of Biomedical Engineering, Department of Pharmaceutics, Purdue University, W Lafayette, IN 47907, USA

E-mail: sangyoup@purdue.edu, cpaul@purdue.edu, kpark@purdue.edu and jpr@flocyt.cyto.purdue.edu

Received 17 November 2006, in final form 5 June 2007
Published 6 July 2007
Online at stacks.iop.org/JMM/17/1558

**Abstract**
A mononuclear compound droplet generation system has been developed based on both the hydrodynamic flow focusing and the solvent exchange method. The results show that the current system provided excellent control over the jet diameters of individual fluid consisting of the compound jet and the resultant compound drop diameters. The compound droplets were controlled in the range of 46–90 $\mu$m. The synchronous jet breakup for the mononuclear compound drop generation occurs where $x \lesssim 0.61$ and $x \lesssim 0.76$, respectively, for the inviscid and viscous capillary velocities. Also, the effect of the solvent diffusion during the jet breakup process and the shear stress on the compound droplet were investigated.

(Some figures in this article are in colour only in the electronic version)

## 1. Introduction

The encapsulation of micro/nano-sized droplets has been of great interest for many industrial and scientific applications. Various methods have been attempted recently for microencapsulation such as droplet collision using an inkjet nozzle [1], coaxial atomizer [2, 3], coaxial electrospray [4–6], spray drying [7], emulsification [8] and hydrodynamic focusing [9, 10]. These encapsulation technologies basically generate double emulsions by breaking up two different bulk fluids into the desired small volumes, i.e. in the third medium. All these methods basically show a controllable manufacturing process for shell-type microcapsules over the conventional double emulsion process based on the mechanical agitation of massive fluids [11–13] which results in a large amount of wasted materials, wide (or random) size distribution and low encapsulation efficiency.

Microencapsulation is frequently employed to achieve long-term drug delivery which typically leads to the formation of a polymer matrix containing dispersed drugs. Recently, a large number of protein drugs have been encapsulated in microspheres. Proteins are high molecular weight compounds that possess very complex and delicate globular structures with unique properties. The three-dimensional structure of proteins can range from approximately 2 to 14 nm [14]. The complex high-order architecture of the protein molecule, which has many chemically labile bonds and reactive side-chain moieties, dictates its specific biological function [15]. When this complex structure is even slightly altered, bioactivity can be lost. To protect the fragile protein molecular structure, it is advantageous to avoid conditions stressful to proteins, such as high mechanical stress as in the conventional double emulsion process. Protein drugs, which are also prone to degradation by enzymes, can be protected by microencapsulation inside the inert polymer membrane such as poly(lactide-co-glycolide) (PLGA) [16, 17]. Among a number of polymer membrane formation techniques, a promising mechanism, so-called *solvent exchange method*, has been introduced by Yeo *et al*

[18, 19]. In this method, a water-insoluble polymer such as PLGA is dissolved in a hydrophilic organic solvent such as methyl or ethyl acetate. When this polymer solution comes in contact with an aqueous solution, the solvents undergo bi-directional mass transfer based on molecular diffusions at the interface between the organic and aqueous phase. As a result, PLGA undergoes a precipitation process leading to the formation of reservoir-type microcapsules [18, 19].

The classic mechanism of drop formation through jet breakup lies under Rayleigh instability or capillary instability. Analysis shows that the axisymmetric disturbances on an inviscid liquid jet affected by surface tension under laminar flow conditions grow only if the wavelength is longer than the circumference of the jet [20, 21]. Experimental studies on two-layered compound jet instability were performed by Hertz and Hermanrud [22] and showed that the velocity gradient and the large shear forces between jet-forming fluids could be sources of the compound jet instability other than the capillary instability. Also it has been shown that the drop formation mechanism in the compound jet due to the capillary instability is identical to that in the conventional jet.

The compound jet breakup has been used for microcapsule generation by several research groups. Loscertales *et al* [6] introduced an encapsulation method in which the two-layer compound jet breaks up in the air under electro-hydrodynamic forces. This technique involves flow focusing established by the electro-hydrodynamic forces. One disadvantage of this technology is that the fluids need to be conductive. Gañán-Calvo *et al* [24] generated mono-dispersed air bubbles in the micron scale using capillary flow focusing. A much faster breakup of the air stream within the liquid jet was observed due to the large property difference between two fluids. This system is similar to a conventional flow cytometry with a jet-in-air-type flow chamber, except the capillary delivers air instead of sample solution. Bocanegra *et al* [23] showed a microencapsulation method using a compound jet formed through hydrodynamic focusing. In their research, the photosensitive polymer was used to encapsulate water-based ink. The jet breakup was modulated using the waveform generator and monodispersed multinuclear microcapsules were successfully acquired. Utada *et al* [10] developed a micro device for double emulsion generation using the high viscosity contrast between the sheath fluid and the jetting fluids. In order to make the compound jet behave like a jet composed of only one component, viscosities of the jetting fluids were matched. Higher viscosity of sheath fluid exerts viscous stress on the compound jet and under high viscous stress the compound jet breakup occurs.

The difficulties of mononuclear compound drop formation lie in matching the breakup timing of each component of the jet because the wavelength response related to the perturbation is a function of the fluid properties [25]. A couple of methods can be used to treat the compound jet close to a single jet. One method is to match the viscosities of fluids consisting of the compound jet, as described above, so that a smooth velocity profile across the interface of the compound jet can be acquired [10]. Another method is to control the thickness of the outer fluid of the compound jet. When the thickness of the polymer solution in a compound jet is thinner relative to the core fluid thickness, the jet instability of the core fluid begins to dominate the instability of the compound jet from a certain thickness [26]. An additional problem is solvent diffusion. Since solvent exchange between water and solvent induces the coacervation process during the compound jet and drop formations, jet breakup dynamics, i.e. instability, becomes more complicated.

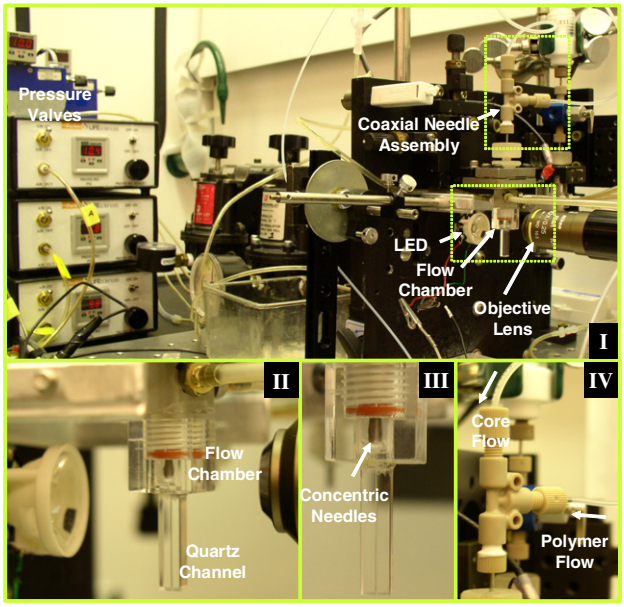


**Figure 1.** System for microcapsule generation. (I) Experimental setup in a chemical hood. (II) Close view of the flow chamber and the 250 $\mu$m square microchannel. (III) Tip of the coaxial needle assembly is located in front of the quartz channel inlet. (IV) Coaxial needle assembly. The corrugated outer needle enforces the coaxial alignment with the inner needle. $1/32''$ OD and $1/16''$ OD stainless steel needles are connected with a tee.

In the current study, the jet breakup mechanism of the two-layered compound jet was experimentally investigated in a co-flowing third medium (distilled water) for mononuclear compound droplet generation. The compound jet was generated using both hydrodynamic focusing and a coaxial tubing setup built upon the conventional flow cytometer. The coaxial compound jet consists of the aqueous core fluid (distilled water) and the biodegradable surrounding polymer solution (PLGA in ethyl acetate). Control over the compound droplets and the core sizes was accomplished using individual flow rate control. The effect of the polymer solution flow rate on the compound jet breakup process and the compound drop size was studied through comparison of the capillary velocity of the core jet and the polymer solution.

## 2. Experimental setup and working principle

The microcapsule generation system was built upon conventional flow cytometry technology. The overall experimental setup is shown in figure 1(I). The whole system was installed on an optical table with the vibration isolation mount in a chemical hood. The two main components of the drop generation are the *flow chamber* shown in figures 1(II) and (III) and the coaxial needle assembly shown in figure 1(IV). The first modification on the conventional flow cytometer was made on the insertion needle which

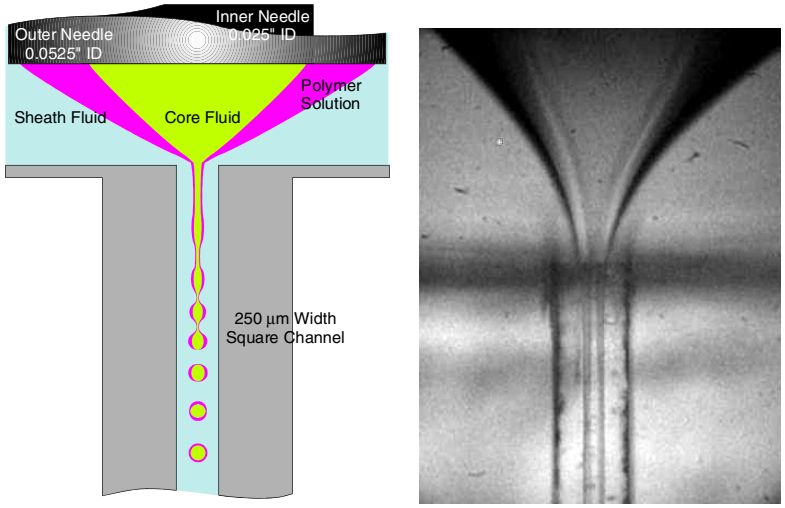


(*a*) (*b*)

**Figure 2.** Schematic diagram (*a*) and photo (*b*) of the hydrodynamic focusing region and the compound jet formation. Note: ∼2 mm from the microchannel inlet was obscured later in the experiment to secure the leakage.

delivers the sample solution in the flow cytometer. In order to generate a compound jet, a coaxially aligned stainless capillary set replaced the single insertion needle of the flow cytometer. These capillaries were connected with PEEK tee and the alignment of two capillaries was acquired using a corrugated outer capillary. Relatively large capillaries were used in order to install two capillaries satisfying the existing system configuration. The dimensions of the inner and outer capillaries are $1/32''$(OD)–$0.025''$(ID) and $1/16''$(OD)–$0.0525''$(ID), respectively. The second modification was made on the flow chamber. In order to acquire optical access without distortion, the flow chamber was built in a cubic form rather than in the conical form of the flow cytometer with transparent acrylic. Clear windows were made on four sides to allow optical access for investigating the hydrodynamic focusing region. Lastly, a square microchannel (250 $\mu$m × 250 $\mu$m × 20.3 mm) for the co-flowing fluid was installed as an exit of the flow chamber in order to simplify the jet breakup mechanism or the compound jet instability. Because the co-flowing sheath fluid is confined within the channel, the perturbation, which would grow on the interface between the sheath and the outer medium, e.g. air without the microchannel boundary, is no longer a concern, but is rather a developing flow problem.

Precise flow rate controls were required in order to obtain the desired mononuclear profiles of the droplets. All working fluids, i.e. the sheath fluid, the polymer solution and the core fluid, were driven by compressed air controlled with four digital pressure valves (VSO-EP, Parker Hannifin Co.). Because the profiles of the compound droplets are closely related to the coaxial stream formation from the flow chamber, the hydrodynamic focusing region in the flow chamber was monitored with a CCD (charge-coupled device) camera (Retiga 4000R, Qimaging Co.) to ensure that the pressure balance between two adjacent fluids was optimal. The compound jet breakup in the square microchannel was also monitored using the CCD camera with a strobe light. Because the minimum exposure time of the CCD camera was short enough, 10 $\mu$s, the still images of the compound droplets flowing with an average velocity of ∼3–5 m s$^{-1}$ were acquired by illuminating the flow field in the microchannel with a short pulse of light (0.1–0.2 $\mu$s). Both the CCD camera (Retiga 4000R, Qimaging Co.) and strobe light (Luxeon III Star, Lumileds Lighting LLC) were externally operated under synchronization of the signals from the pulse generator (Berkeley Nucleonics Co.).

The flow chamber is where the fluids in macroscale transform into the microscale so that they can be readily disintegrated into the small volumes desired. This transformation was made using hydrodynamic focusing in the flow chamber. Figure 2 shows a schematic diagram and a photo of the flow field in the flow chamber and the microchannel. A coaxial stream consisting of the polymer solution and the core fluid was fed into the flow chamber through a coaxial stainless-steel capillary assembly. Sheath fluid was supplied directly into the flow chamber as in a conventional flow cytometer. In order for mass conservation to be satisfied, the sheath fluid and the coaxial stream were accelerated into the microchannel forming a cone shape in front of the microchannel inlet, a so-called *hydrodynamic focusing region* [9]. Inside the flow chamber, all flows were absolutely stable and thus the shape of the coaxial stream depended only on both the fluid properties and the driving pressures. In the quartz channel, the coaxial stream formed a compound jet. The perturbation then expanded on the compound jet surface and after the compound jet grew sufficiently, disintegration occurred under the dominating instability within the microchannel.

The jet breakup process greatly depends on the fluid properties such as density, viscosity and interfacial tension. In order to have the compound jet behave like a single jet, 3% (w/v) PLGA solution was chosen to closely match the viscosity with those of the sheath and the core fluids. Since 3% PLGA solution showed the largest viscosity among the working fluids, the flow rate of the polymer solution was chosen as a varying parameter. The driving pressures of the

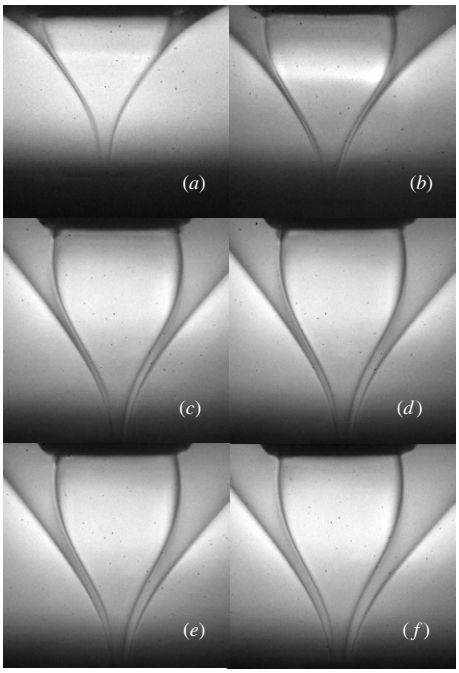


**Figure 3.** The shapes of fluid cones inside the flow chamber. $Q_P/Q_{Tot}$ are (*a*) 0.0044, (*b*) 0.0099, (*c*) 0.0207, (*d*) 0.0277, (*e*) 0.0316 and (*f*) 0.0377, respectively. For (*a*) and (*b*), the coaxial tube was moved slightly toward the square channel entrance.

**Table 1.** Properties of working fluids at 25 °C.

| | $\rho$ (kg m$^{-3}$) | $\mu$ (cP) | $\gamma$ (dynes cm$^{-1}$) |
|---|---|---|---|
| Water | 997.1[a] | 0.890[a] | – |
| Ethyl acetate (EA) | 884.8 | 0.480 | 6.80[b] with water |
| 3% (w/v) PLGA in EA | 894.6 | 1.237 | – |

[a] and [b] are from [27] and [28], respectively, and others are measured values.

sheath and the core fluids were kept constant at 5.2 psig and the PLGA flow rates were varied from 5.1 to 5.5 psig. The flow rate of the sheath fluid was measured with a rotameter, while the flow rates of the polymer solution and the core fluids were measured using the weighing balances. The Reynolds number based on the sheath flow rate was ~1100, i.e., laminar flow. The fluid properties in the current study are listed in table 1. Because the interfacial tension between the polymer solution and water was unknown, the value for ethyl acetate and water was used for analysis purposes [29].

## 3. Results and discussion

### *3.1. Compound jet formation*

The effects of flow rate (or pressure) controls on the fluid geometry inside the flow chamber, i.e. the coaxial cone shape, are shown in figure 3. In order to avoid the back flow of the sheath fluid into the coaxial needle, the exit of the coaxial needle was located within the hydrodynamic flow focusing region where the pressure gradient becomes greater. For figures 3(*a*) and (*b*), the coaxial needle exit was moved downward slightly to ensure that the exit of the coaxial needle was located within the hydrodynamic focusing region. Once the coaxial needle was located in the hydrodynamic flow focusing region, the coaxial cone was absolutely stable. The clear increases in the thickness of the polymer solution are shown with the driving pressure of the polymer solution. Interestingly, the volume of the core fluid appears to increase gradually through figures 3(*a*)–(*c*), but the significant increase was not observed in figures 3(*c*)–(*f*). Since the pressures of the sheath and the core fluids were kept constant, the cross-sectional area of each fluid at the entrance of the square microchannel was set by the flow rate (or driving pressure) of each fluid. The cross-sectional area of each fluid was insensitive to the location of the coaxial needle exit as long as the coaxial needle exit was located within the hydrodynamic focusing region. This is likely because the resulting cross-sectional area of each fluid is more dependent on the interfacial tension and the density and flow rate ratios between the adjacent fluids.

In order to find the jet diameter theoretically, the pressure drop of each fluid between s′–s, p′–p and c′–c, see figure 4, was calculated. The potential flow assumption was made within the flow chamber. Thus, the pressure drop from s′, p′ and c′ to the microchannel inlet was calculated using the Bernoulli equation [9, 24]. The potential flow assumption in the flow chamber is reasonable because the viscosity difference of each fluid is small and the acceleration of each fluid is virtually uniform in the hydrodynamic focusing region. The additional pressure loss due to wall friction was considered for the sheath fluid from the microchannel inlet to the position where the jet diameter was measured using Poiseuille's equation; thus, the viscosity effect was only considered within the microchannel. For the additional pressure drop of sheath flow, the cross-sectional area of the compound jet was considered smaller than the microchannel's and neglected in calculation.

The jet diameters in the square channel were found theoretically using the pressure balance across the interface with the *Young–Laplace* relation between the sheath fluid and the compound jet [24] and the resulted expression is

$$d^{-4} + \left(\frac{\pi^2\gamma}{2\rho_j Q_j^2}\right) d^{-1} = \frac{\pi^2}{16D^4}\left[\left(\frac{\rho_s Q_s^2}{\rho_j Q_j^2}\right) + \left(\frac{256 Q_s \mu_s \chi}{\rho_j Q_j^2 \pi}\right)\right], \quad (1)$$

where $\rho$, $\gamma$, $Q$, $D$ and $d$ are, respectively, the density, the interfacial tension, the flow rate, the width of the square channel and the jet diameter. $\chi$ is the distance from the square channel entrance to the position where the jet diameters were measured. The subscripts $j$ and $s$ represent jet and sheath, respectively. For the compound jet diameter calculation, the compound jet was considered as a single jet formed with the polymer solution only. The pressure balance was made at the interface between s and p. On the other hand, for the core jet diameter, the polymer solution was considered as the sheath fluid and the pressure balance was made at the interface between p and c.

Figure 5 shows the compound and core jet diameters and the measured flow rates of the sheath and core fluids. The jet diameters were measured from the captured images at the axial distance ~4 mm from the microchannel inlet. The measured and calculated jet diameters show very good agreement and

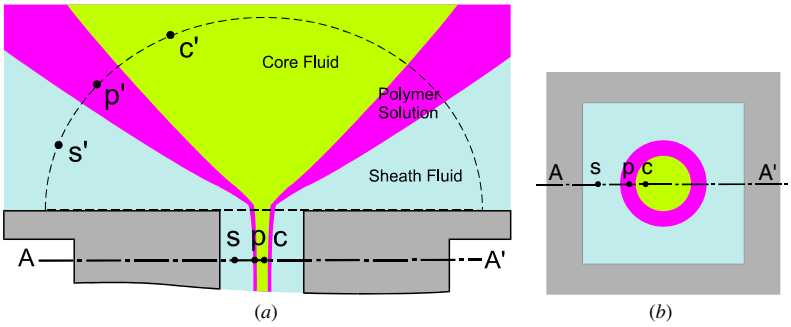


**Figure 4.** Schematic diagrams of the hydrodynamic focusing region (*a*) and the cross-sectional area of the square channel on the A–A′ plane (*b*). The dashed line indicates a virtual iso-pressure line in the hydrodynamic focusing region. The symbols s, p and c represent the sheath fluid, the polymer solution and the core fluid, respectively.

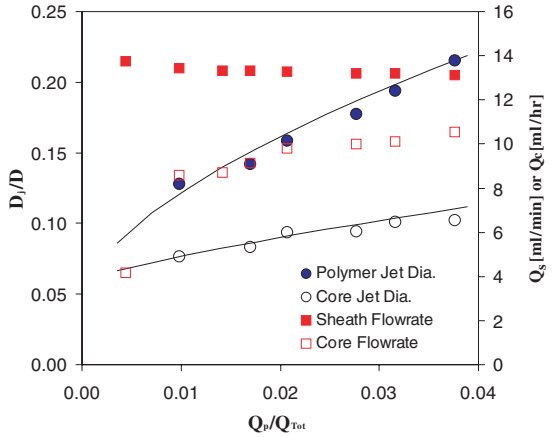


**Figure 5.** Compound and core jet diameters and the flow rates of the sheath and core fluids. The solid lines are the analytically calculated jet diameters using equation (1). Note: the units for the sheath and the core fluid flow rates are different.

the assumptions made in equation (1) seem valid. The increase of polymer solution flow rate increases the core jet diameter as well as the compound jet diameter, though the core jet diameter increases very slowly. The polymer solution flow rate affects the cross-sectional area of both the sheath and core fluids at the microchannel inlet. With the increase of the polymer solution flow rate, the sheath flow rates show the gradual decrease while the core flow rate increases. That is, the increase in the polymer solution flow rate reduces the cross-sectional area of the sheath fluid rather than that of the core fluid because the interface between p and c is exposed to the greater pressure than the interface between s and p due to the larger radius of curvature.

### *3.2. Compound jet breakup*

The compound droplet profiles depend on the breakup pattern of the compound jet. For mononuclear drop formation, the synchronized undulation of both core fluids and polymer solution is required. Unless the properties of two fluids are exactly identical so that the compound jet behaves like a single jet, the undulation can be asynchronous. Suryo *et al* [30] extensively performed the finite element numerical analysis on the compound jet breakup with respect to the various parameters, such as density, viscosity, interfacial tension and radius ratios, showing qualitatively good agreements with the current experiments.

Figure 6 shows the jet breakup pattern at $Q_P/Q_{\mathrm{Tot}} = 0.0099, 0.0142, 0.0170, 0.0277$ and $0.0377$, respectively. The undulations on the surfaces of the compound jet result in both the primary compound droplets (PCD) and the satellite compound droplets (SCD). In all cases, the core satellite drops (CSD) seem to undergo a further breakup process and to generate one or two child core satellite drops (CCSD). The child core satellite drops appear in the primary compound drops or/and in the satellite compound drops depending on the breakup conditions. Thus, the primary compound droplets consist either of *single* core primary drop (CPD) or of *single* core primary drop and *single* or *multiple* satellite drops of the core fluid, i.e. (child) core satellite drop. Similarly, the satellite compound droplets consist either of *single* satellite drop of core fluid or of *single* satellite drop of core fluid and the child core satellites drops. This compound jet breakup pattern agrees with the numerical results by Suryo *et al* [30]. In their analysis for the radius ratio $d_{j,p}/d_{j,c} = 2$ and the interfacial tension ratio $\gamma_p/\gamma_c = 2$, the compound drop formation is favored at low Reynolds numbers where the reduced wave number $x_c$ $(=\pi d_c/\lambda) \lesssim 0.5$ for $Re_c$ $(=\sqrt{\rho_c\gamma_c d_c}/2\mu_c) \leqslant 10$. Large satellite drops were generated regardless of whether compound drops were formed for such a small wave number range, where $d$, $\lambda$, $\rho$, $\gamma$ and $\mu$ are the jet diameter, wavelength, density, interfacial tension and dynamic viscosity, respectively, and the subscripts $p$ and $c$ indicate the polymer solution and the core fluid, respectively. In the current fluidic system, the Reynolds number for the core jet was found to be $0.21 \leqslant Re_c \leqslant 0.24$. The diameter, reduced wave number and interfacial tension ratios were found to be $1.68 \leqslant d_{j,p}/d_{j,c} \leqslant 2.11$, $0.33 \leqslant x_c \leqslant 0.38$ and $\gamma_p/\gamma_c = 1$, respectively.

The time scale on which the surface perturbation grows very much depends on the flow system. For the system where the viscosity of outer fluid is larger than that of the jetting fluid, the velocity scale can be represented with the viscosity of the outer fluid and the interfacial tension such as $\gamma/\mu$ resulting in the time scale as $\mu/\gamma$ [31]. Powers *et al* [31] provided the proportional constant for various viscosity ratios. The time scale ($t_{\mathrm{cap,vis}}$) was given as $C\mu_s d_j/2\gamma$, where $d_j$ is the jet diameter and the subscript $s$ indicates the sheath [31]. When the jet of low viscosity is formed in a vacuum, the instability is considered to be mainly caused by the surface tension. In this case, the velocity scale of $\sqrt{2\gamma/\rho d_j}$ and the time scale

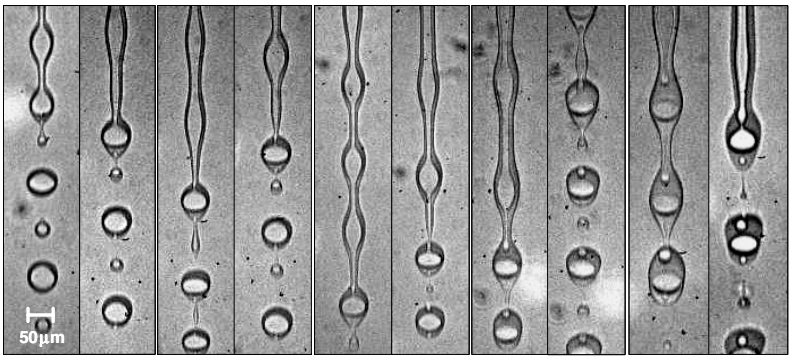


**Figure 6.** Compound jet breakup patterns at various flow rates of the polymer solution. $Q_P/Q_{\mathrm{Tot}}$ are (*a*) 0.0099, (*b*) 0.0142, (*c*) 0.0170, (*d*) 0.0277 and (*e*) 0.0377. The image of compound jet breakup at the $Q_P/Q_{\mathrm{Tot}} = 0.0044$ case was not provided because the breakup length was very short and the breakup occurs within the region where the optical access is limited.

($t_{\mathrm{cap,inv}}$) of $\sqrt{\rho d_j^3/8\gamma}$, where $\rho$ is the density, are found from the balance of the inertia and the surface tension forces [32]. The actual jet breakup time is much longer than these capillary times [30]. However, the capillary times for core and polymer jets are still useful for the determination of the compound drop formation through the comparison such that the compound jet undergoes synchronous jet breakup when these two capillary times match. According to Suryo *et al* [30], the breakup time of a compound jet with $\gamma_p/\gamma_c = d_{j,p}/d_{j,c} = 2$ and $\rho_p/\rho_c = 1$ is insensitive to the viscosity ratio where $\mu_p/\mu_c < 1$. The compound drops were formed at $10^{-3} < \mu_p/\mu_c < 10$ at $Re_c = 1$. The effect of interfacial tension ratio was shown at $x_c = 0.3$ for $d_{j,p}/d_{j,c} = 2$ and $\rho_p/\rho_c = \mu_p/\mu_c = 1$ such that the compound drops were formed where $\gamma_p/\gamma_c > 1$. In the current system, the interfacial tension ratio was kept to 1 and the viscosity ratio ($\mu_p/\mu_c$) and the Ohnesorge number, $Oh$ ($=t_{\mathrm{cap,vis}}/t_{\mathrm{cap,inv}}$), were found to be 1.39 and 0.75–0.98, respectively. Since both viscosity and inertia play considerable roles in the jet breakup process, the breakup condition was studied by observing both viscous and inviscid capillary velocities, $\sim\gamma/\mu$ [10, 31] and $(2\gamma/\rho d_j)^{1/2}$ [32].

Figure 7 shows the capillary time with respect to the reduced wave number, $x_i = \pi d_{j,i}/\lambda$, where $\lambda$ is the distance between the primary compound droplets and $d_{j,i}$ is the compound jet diameter. The subscript $i$ can be either $p$ or $c$ indicating polymer and core solutions, respectively. For a polymer solution, the jet radius was defined as $(d_{j,p} - d_{j,c})/2$. The solid and the dashed lines indicate the second-order polynomial curve fittings for the inviscid and the viscous cases, respectively. The proportional constant, $C$, in the viscous capillary time scale was given as $\sim 100$ for the unity viscosity ratio to the stationary outer fluid [31]. In the current experiment, however, the proportional constant $C$ was chosen to be 10 because the viscous capillary time showed better agreement with the inviscid capillary time at $C = 10$ than at $C = 100$; $C = 100$ results in the unrealistically large capillary time scale. The capillary time for the polymer solution increased with the reduced wave number almost linearly both for the viscous and inviscid capillary times. The inviscid capillary time increased much faster than the viscous capillary time, which suggests that disintegration from the jet occurs quickly due to the presence of the co-flowing sheath

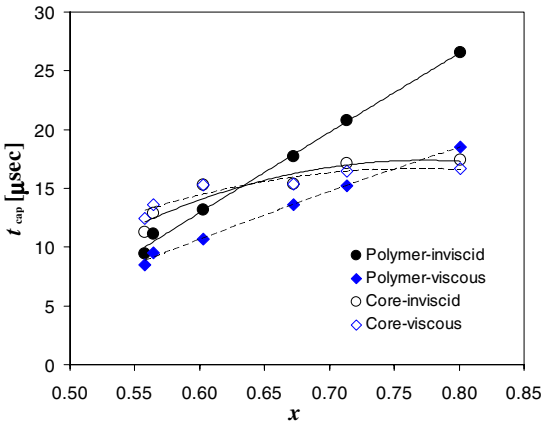


**Figure 7.** Capillary time of the compound jet with respect to the reduced wave number, $x = \pi d_j/\lambda$. ● and ○ are the inviscid capillary times, $t_{\mathrm{cap}} = (\rho r_j^3/\gamma)^{1/2}$, for the polymer solution and the core fluid, respectively. ♦ and ◊ are the viscous capillary times, $t_{\mathrm{cap}} = C\mu r_j/\gamma$, for the polymer solution and the core fluid, respectively. Note: for polymer solution, the jet radius of $(r_{j,p} - r_{j,c})$ has been used.

fluid. Though the driving pressure for the core fluid was kept constant, $t_{\mathrm{cap}}$ for the core fluid showed a gradual increase with reduced wave number identifying a plateau where $x \geqslant 0.65$.

Interestingly, both viscous and inviscid cases showed that the core fluid pinched off quicker than the polymer solution at the beginning. For the inviscid case, the differences of $t_{\mathrm{cap}}$ for the polymer solution and the core fluid were small at the beginning and this difference increased rapidly. On the other hand, the viscous case showed the opposite behavior. At the beginning, $t_{\mathrm{cap}}$ of the core fluid and the polymer solution showed the large difference and the difference decreased with the reduced wave number. In both cases, the capillary times for the polymer solution and the core fluid cross each other, that is, the inversions of the capillary time, at $x_i \approx 0.76$ for the viscous capillary time scale and at $x_i \approx 0.63$ for inviscid capillary time scale, respectively. Suryo *et al* [30] also pointed out that the outer interface may break before the inner one when the thickness of the shell fluid continues to decrease.

Comparison between figures 6 and 7 was made to investigate the relations between the jet breakup pattern and the

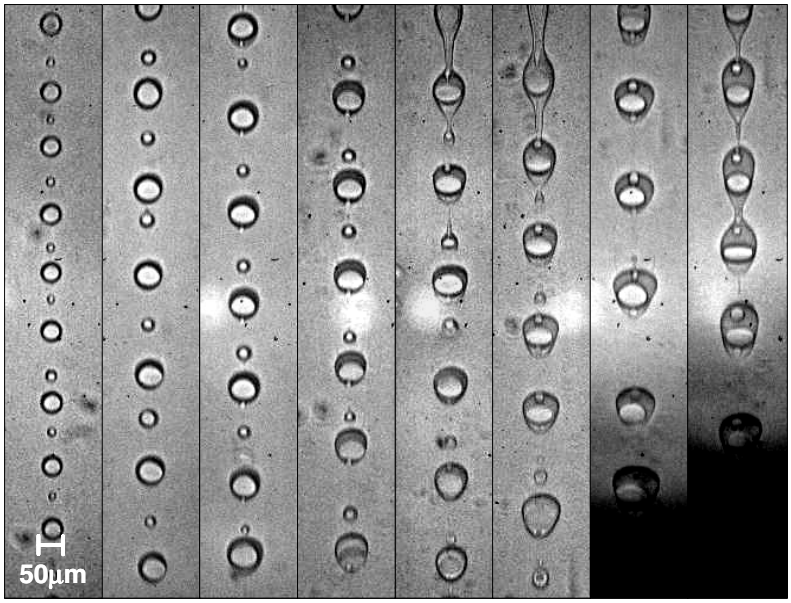


**Figure 8.** Photos of compound droplets generated within the square channel. $Q_p/Q_{\mathrm{Tot}}$ are (*a*) 0.0044, (*b*) 0.0099, (*c*) 0.0142, (*d*) 0.0170, (*e*) 0.0207, (*f*) 0.0277, (*g*) 0.0316 and (*h*) 0.0377, respectively. For (*g*) and (*h*), the compound droplets exit the microchannel.

capillary time. With the inviscid capillary time, the inversion at $x_i \approx 0.63$ signifies that the pinching-off of the polymer solution layer occurred slightly earlier than that of the core fluids where $x \leqslant 0.63$ corresponding to the case (*a*)–(*c*) in figure 6. The viscous capillary time scale estimates the inversion at $x_i \approx 0.76$. Thus, the reduced wave number at the inversion is supposed to be located between cases (*d*) and (*e*) of which $x = 0.672$ and 0.801, respectively. However, figure 6(*d*) shows that the disintegration of the core fluid within the polymer solution and the inversion occurred already at $x = 0.672$. In figure 6(*e*), corresponding to $x = 0.801$, core satellite drops were formed within the polymer solution.

*3.2.1. Effect of solvent exchange on compound jet instability.* From figures 6 and 8, the compound jet breakup process appears not to be dependent upon the diffusion of solvent. In fact, the diffusion in the polymer solution is typically slower than that in the nonsolvent phase. The typical values are found as $\sim 1 \times 10^{-6}$ cm$^2$ s$^{-1}$ for the diffusion in the polymer solution and as $\sim 1 \times 10^{-5}$ cm$^2$ s$^{-1}$ for the diffusion in the nonsolvent phase based on the assumption of the constant properties [33, 34]. In particular, the diffusion coefficient of the pure ethyl acetate into water is $\sim 1.12 \times 10^{-5}$ cm$^2$ s$^{-1}$ [35]. At a flow rate of 13 ml min$^{-1}$, the sheath fluid takes about 3.5 ms from the microchannel inlet to the outlet. In this case, the mean diffusion length is less than $\sim 3$ $\mu$m which is about 10–20% of the polymer solution thickness. In addition, the jet breakup actually occurs within the microchannel, 5–8 mm from the inlet. Therefore, the effect of solvent diffusion on the jet breakup pattern must be minimal.

### *3.3. Compound drop diameter*

Rayleigh jet breakup generates fairly uniform droplets. Figure 8 shows photos of both the primary and satellite compound droplets generated through a compound jet breakup surrounded with water flow in a square channel at several flow rate combinations. The flow rates of the polymer solution with respect to the total flow rates, $Q_p/Q_{\mathrm{Tot}}$, are varied by adjusting the driving pressure, from left to right, 0.0044, 0.0099, 0.0142, 0.0170, 0.0207, 0.0277, 0.0316 and 0.0377, respectively.

Fairly well-defined primary and satellite compound droplets were observed (see figures 8(*a*)–(*e*)). At the slowest flow rate, $Q_p/Q_{\mathrm{Tot}}$ equals (*a*) 0.0044, the child core satellite drops were not observed; the primary and satellite compound drops show mononuclear compound drop generation. The child core satellite drops start to appear from $Q_p/Q_{\mathrm{Tot}}$ equal to (*b*) 0.0099 either in the primary compound drops or in the satellite compound drops. At this flow rate, a single child core satellite drop is formed and thus the mononuclear primary compound drops are intermittently observed in figure 8 child core satellite drops are enclosed in the satellite compound drops; the corresponding breakup pattern was shown in figure 6(*a*). At $Q_p/Q_{\mathrm{Tot}}$ equal to (*c*) 0.0142, the mononuclear primary compound drops are not observed because the child core satellite drops are kept enclosed in the primary compound droplets, which was also observed from the jet breakup process in figure 6(*b*). The presence of the multiple child core satellite drops was shown from $Q_p/Q_{\mathrm{Tot}} = 0.0170$ in figure 6(*c*). In figure 8, at $Q_p/Q_{\mathrm{Tot}} =$ (*d*) 0.0170 and (*e*) 0.0207, the multiple child core satellite drops appear both in the primary compound drops and in the satellite compound drops. The core satellite droplets are enclosed in the satellite compound droplets up to $Q_p/Q_{\mathrm{Tot}} =$ (*e*) 0.0207 ($x \approx 0.603$). However, from $Q_p/Q_{\mathrm{Tot}} =$ (*f*) 0.0277, the disintegration of core primary drop occurs within the undulating polymer stream and the core satellite drops are now shown in the primary compound droplets and the child core satellite drops appear in the satellite compound drops. This confirms that the asynchronous jet breakup occurs after the inversion of $t_{\mathrm{cap}}$ of the core fluid and the polymer solutions at $x_i \approx 0.61$ as shown in figure 7.

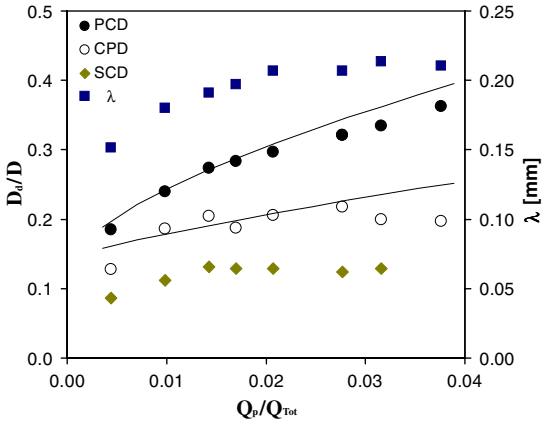


**Figure 9.** Primary and satellite compound drop diameters, the core primary diameter and the distance between the primary compound drops with respect to the reduced wave number.

Drop diameter was simply predicted with the assumption of no satellite drop generation using the mass conservation as

$$d_d = \left(\frac{6Q}{\pi f}\right)^{1/3}, \tag{2}$$

where $Q$ and $f$ are the flow rate and the drop generation frequency, respectively. Because the imposed frequency was absent, the drop generation frequency depends on the fluid properties and the flow condition [25] and was found based on $\lambda$ and the jet velocity. The diameter changes of the primary and satellite compound droplets and the core primary drops predicted with equation (2) were compared with the experimental results in figure 9. The solid and dashed lines represent the diameters of the primary compound drop and the core primary drop calculated using equation (2). The drop diameters were graphically measured from the acquired images and the calculations for the solid and dashed lines were made based on the inviscid and the viscous capillary velocity scales defined as $(2\gamma/\rho d_j)^{1/2}$ and $\gamma/\mu$, respectively.

Figure 9 shows that the estimations are in fairly good agreement with the experimental results. The diameter of the primary compound drop gradually increased with $Q_p/Q_{\mathrm{Tot}}$, which appeared similar to the jet diameter changes shown in figure 5. Both analytical results predict drop diameters close to the experimental results at the first three flow rates, $Q_p/Q_{\mathrm{Tot}} =$ 0.0044–0.0142. As $Q_p/Q_{\mathrm{Tot}}$ increased, the analytical results estimate the greater drop diameters at $Q_p/Q_{\mathrm{Tot}} =$ 0.0277–0.0377. The viscous capillary time-based estimation with the proportional constant $C = 10$ showed a good agreement with the experimental results and the assumption of the shorter capillary time due to the co-flowing sheath fluid seems valid. The increase of the core primary drop size is much slower compared to the increase of the primary compound drop diameter. For the core primary drop, both analytical calculations agree well with each other, but predict a drop diameter less than the experimental results around $Q_p/Q_{\mathrm{Tot}} =$ 0.0099–0.0277. The experimental results show that the drop diameter increases up to $Q_p/Q_{\mathrm{Tot}} = 0.0142$ and stays almost invariant. This agrees with the flow rate and the jet diameter changes of the core fluid observed in figure 5. The flow rate of the core fluid increased quickly at the beginning with the flow rate of the polymer solution and slowed the slow increase because the cross-sectional change of the polymer solution at the microchannel inlet is toward the sheath fluid side. For the satellite compound drops, the drop diameter shows similar trend to the core primary drop diameter, increases up to $Q_p/Q_{\mathrm{Tot}} = 0.0142$ and stays almost invariant. The satellite compound drops were irregularly formed at higher flow rates, $Q_p/Q_{\mathrm{Tot}} = 0.0316$ and 0.0377. This irregular satellite compound drop formation and the invariant drop diameters at higher flow rate seem from the asynchronous jet breakup; the satellite compound drops enclose the child core satellite drops rather than the core satellite drops.

## 4. Conclusion

A reliable method based on both the hydrodynamic flow focusing and the solvent exchange method has been proposed for compound droplet generation. The compound droplet diameter was very much controllable by adjusting the polymer thickness through a precise pressure controlled flow system. The sizes of compound droplets were controlled in the range of 46–90 $\mu$m while the core size ranged around 30–50 $\mu$m. Compound jet instability for mononuclear compound droplet generation was investigated in the co-flowing medium. The co-flowing environment was established using a square microchannel. Analytical estimation of the compound jet was made based on both the potential flow and Poiseuille flow assumptions in the flow chamber and microchannel, respectively. Analytical estimation showed very good agreement with the experimental results. The synchronous jet breakup occurred where $x \lesssim 0.63$ and $x \lesssim$ 0.76, respectively, for the inviscid and viscous capillary velocities. Solvent diffusion appears to have the minimal effect on the jet breakup process; the estimated diffusion time of the pure ethyl acetate into water was much longer compared to the capillary times. It has been shown that the profile of the compound droplet was greatly dependent on the compound jet breakup process. When the compound jet breakup was synchronous, mononuclear compound droplets were acquired. Shear stress from the sheath fluid seems to enhance the compound jet breakup process resulting in a drop diameter reduction.

## Acknowledgments

This study was supported by the National Institute of Health through grants GM67044 and EB003584. The authors are thankful for the support from Parker Life Sciences Co. and QImaging Co.

## References

[1] Yeo Y, Basaran O A and Park K 2003 *J. Control. Release* **93** 161–73
[2] Yeo Y and Park K 2004 *J. Control. Release* **100** 379–88
[3] Berkland C, Pollauf E, Pack D W and Kim K K 2004 *J. Control. Release* **96** 101–11
[4] Gañán-Calvo A M 1997 *J. Fluid Mech.* **335** 165–88
[5] Gañán-Calvo A M, Davila J and Barrero A 1997 *J. Aerosol Sci.* **28** 249–75
[6] Loscertales I G, Barrero A, Guerrero I, Cortijo R, Marquez M and Gañán-Calvo A M 2002 *Science* **295** 1695–8

[7] Freitas S, Merkle H P and Gander B 2004 *J. Control. Release* **95** 185–95
[8] Liu R, Ma G H, Meng F T and Su Z G 2005 *J. Control. Release* **103** 31–43
[9] Gañán-Calvo A M 1998 *Phys. Rev. Lett.* **80** 285–8
[10] Utada A S, Lorenceau E, Link D R, Kaplan P D, Stone H A and Weitz D A 2005 *Science* **308** 537–41
[11] Hildebrand G E and Tack J W 2000 *Int. J. Pharm.* **196** 173–6
[12] Reithmeier H, Herrmann J and Gopferich A 2001 *Int. J. Pharm.* **218** 133–43
[13] Freitas S, Merkle H P and Gander B 2005 *J. Control. Release* **102** 313–32
[14] Squire P G and Himmel M E 1979 *Arch. Biochem. Biophys.* **196** 165–77
[15] Schwendeman S P, Cardamone M, Klibanov A, Langer R and Brandon M R 1996 *Microparticulate Systems for the Delivery of Proteins and Vaccines* ed S Cohen and H Bernstein (New York: Dekker) pp 1–49
[16] Uchida T, Yagi A, Oda Y and Goto S 1996 *J. Microencapsul.* **13** 509–18
[17] Park J H, Ye M, Yeo Y, Lee W K, Paul C and Park K 2006 *Mol. Pharm.* **3** 135–43
[18] Yeo Y, Chen A U, Basaran O A and Park K 2002 *29th Int. Symp. on Controlled Release of Bioactive Materials (Seoul, Korea)* pp 547–8
[19] Yeo Y, Kim B Y, Kim J D, Chen A U, Basaran O A and Park K 2002 *29th Int. Symp. on Controlled Release of Bioactive Materials (Seoul, Korea)* pp 549–50
[20] Rayleigh L 1879 *Proc. R. Soc. Lond.* **29** 71–97
[21] Rayleigh L 1879 *Proc. Lond. Math. Soc.* **10** 4–13
[22] Hertz C H and Hermanrud B 1983 *J. Fluid Mech.* **131** 271–87
[23] Bocanegra R, Sampedro J L, Gañán-Calvo A and Marquez M 2005 *J. Microencapsul.* **22** 745–59
[24] Gañán-Calvo A M and Gordillo J M 2001 *Phys. Rev. Lett.* **87** 274501
[25] Elmore W C and Heald M A 1969 *Physics of Waves* (New York: Dover)
[26] Johns L and Narayanan R 2002 *Interfacial Instability* (New York: Springer)
[27] Lemmon E W, McLinden M O and Friend D G 2005 Thermophysical properties of fluid systems *NIST Chemistry WebBook, NIST Standard Reference Database Number 69* (Gaithersburg, MD: National Institute of Standards and Technology) http://webbook.nist.gov
[28] Adamson A W and Gast A P 1997 *Physical Chemistry of Surfaces* 6th edn (New York: Wiley)
[29] Rao N V R and Baird M H I 1983 *J. Phys. E: Sci. Instrum.* **16** 1164–6
[30] Suryo R, Doshi P and Basaran O A 2006 *Phys. Fluids* **18** 082107
[31] Powers T R, Zhang D F, Goldstein R E and Stone H A 1998 *Phys. Fluids* **10** 1052–7
[32] Eggers J 1997 *Rev. Mod. Phys.* **69** 865–929
[33] Reuvers A J and Smolders C A 1987 *J. Membr. Sci.* **34** 67–86
[34] Fernandes G R, Pinto J C and Nobrega R 2001 *J. Appl. Polym. Sci.* **82** 3036–51
[35] Yaws C L 2003 *Yaws' Handbook of Thermodynamic and Physical Properties of Chemical Compounds* (Norwich, NY: Knovel)